INSTITUT DE FRANCE
Académie des sciences

Comptes Rendus

Mécanique

Sven Beuchler, Bernhard Endtmayer, Johannes Lankeit and Thomas Wick

Multigoal-oriented a posteriori error control for heated material processing using a generalized Boussinesq model

Volume 351, Special Issue S1 (2023), p. 111-133

Part of Special Issue: The scientific legacy of Roland Glowinski

Guest editors: Grégoire Allaire (CMAP, Ecole Polytechnique, Institut Polytechnique de Paris, Palaiseau, France),
Jean-Michel Coron (Laboratoire Jacques-Louis Lions, Sorbonne Université)
and Vivette Girault (Laboratoire Jacques-Louis Lions, Sorbonne Université)

https://doi.org/10.5802/crmeca.160

CENTRE
MERSENNE

The Comptes Rendus. Mécanique *are a member of the*
Mersenne Center for open scientific publishing
www.centre-mersenne.org — e-ISSN : 1873-7234

Comptes Rendus
Mécanique
2023, Vol. 351, Special Issue S1, p. 111-133
`https://doi.org/10.5802/crmeca.160`

The scientific legacy of Roland Glowinski / *L'héritage scientifique de Roland Glowinski*

Multigoal-oriented a posteriori error control for heated material processing using a generalized Boussinesq model

Sven Beuchler[a, b], **Bernhard Endtmayer**[a, b], **Johannes Lankeit**[a] and **Thomas Wick**[*, a, b]

[a] Leibniz Universität Hannover, Institut für Angewandte Mathematik, Welfengarten 1,
30167 Hannover, Germany

[b] Cluster of Excellence PhoenixD (Photonics, Optics, and Engineering – Innovation
Across Disciplines), Leibniz Universität Hannover, Germany

E-mails: beuchler@ifam.uni-hannover.de (S. Beuchler),
endtmayer@ifam.uni-hannover.de (B. Endtmayer), lankeit@ifam.uni-hannover.de
(J. Lankeit), thomas.wick@ifam.uni-hannover.de (T. Wick)

Abstract. In this work, we develop a posteriori error control for a generalized Boussinesq model in which thermal conductivity and viscosity are temperature-dependent. Therein, the stationary Navier–Stokes equations are coupled with a stationary heat equation. The coupled problem is modeled and solved in a monolithic fashion. The focus is on multigoal-oriented error estimation with the dual-weighted residual method in which an adjoint problem is utilized to obtain sensitivity measures with respect to several goal functionals. The error localization is achieved with the help of a partition-of-unity in a weak formulation, which is specifically convenient for coupled problems as we have at hand. The error indicators are used to employ adaptive algorithms, which are substantiated with several numerical tests such as one benchmark and two further experiments that are motivated from laser material processing. Therein, error reductions and effectivity indices are consulted to establish the robustness and efficiency of our framework.

Keywords. Boussinesq, finite elements, multigoal error control, partition-of-unity dual-weighted residuals, Y-beam splitter.

Funding. This work has been supported by the Cluster of Excellence PhoenixD (EXC 2122, Project ID 390833453). The second author is supported by an Humboldt Postdoctoral Fellowship.

Manuscript received 10 September 2022, revised 9 December 2022 and 14 December 2022, accepted 15 December 2022.

---

[*] Corresponding author.

1. Introduction

This work considers a nonlinear coupled fluid flow heat system. Fluid flow is described by the incompressible Navier–Stokes equations [1, 2] (for important numerical developments, we refer to [3–11]) and the heat distribution by an advection-diffusion equation. The resulting PDE (partial differential equation) system is known as Boussinesq model [12]. This model has been widely applied in various fields such as climate modeling [13] or earth mantle convection problems [14]. Furthermore, the Boussinesq equation can serve as a sub-model within laser material processing [15] in wave guide modeling (e.g., [16, 17]) where heated material starts to flow due to local heat sources. A mathematical analysis of the stationary model that serves as our point of departure was done in [18].

The objective of this work is to design a robust and efficient framework using adaptive finite elements for the numerical discretization of the Boussinesq system proposed in [18]. Specifically, we derive multigoal a posteriori error estimates with respect to one or several quantities of interest [19–21]. This is intriguing since we deal with a coupled system of partial differential equations in which various parts of the solution might be of interest simultaneously. We notice that related results of coupling the stationary Navier–Stokes equations to the heat equation are published in some conference proceedings and the PhD thesis of the second author [22, 23]. Moreover, there is only one other study [24] in which this multigoal-framework was applied so far to a nonlinear coupled system.

In more detail, we formulate an optimization problem in which the discretization error measured in the goal functional is minimized with respect to a constraint. This constraint is nothing else than the PDE problem itself. For a very detailed description we refer the reader to the introduction of [24]. The resulting optimality system consists of the primal problem (the PDE, here the Boussinesq model) and a linear adjoint problem [25, 26]. These results allow to design error identities and estimators for model errors ([27,28]), discretization and linearization errors [20, 29, 30]. In this work, we consider discretization and linearization errors. In order to use the error estimators for local mesh adaptivity we localize them to single mesh elements using a partition-of-unity localization [31]. This allows us to employ the algorithms from [32] and to apply them in this work to the Boussinseq system. For verification, we use one benchmark and we design two novel prototype experiments. Therein, we study error reductions and effectivity indices.

The outline of this paper is as follows: In Section 2, we explain our problem statement, derive the weak form and briefly explain the finite element discretization. Next, in Section 3, goal oriented adaptivity including multigoal estimates are addressed. Then, in Section 4, we conduct three numerical tests in order to substantiate our algorithmic developments. Our work is summarized in Section 5.

2. Boussinesq model: coupling Navier–Stokes to the heat equation

Let $d = 2$ (we notice that $d = 3$ is possible as well) be the problem dimension and let $\Omega \subset \mathbb{R}^d$ be a bounded domain with boundary $\partial\Omega$. For flow boundary conditions, $\partial\Omega$ is decomposed into non-overlapping parts Γ_{vD} and $\Gamma_{vN} := \partial\Omega \setminus \Gamma_{vD}$, where Γ_{vD} indicate homogeneous or inhomogeneous Dirichlet conditions, respectively, and Γ_{vN} homogeneous or inhomogeneous Neumann conditions, respectively. For the temperature equation, $\partial\Omega$ is decomposed into non-overlapping parts $\Gamma_{\vartheta D}$ and $\Gamma_{\vartheta N} := \partial\Omega \setminus \Gamma_{\vartheta D}$. We note that for each numerical example, we specify the boundaries separately. Moreover, we denote the L^2 scalar product in $L^2(\Omega;\mathbb{R})$, $L^2(\Omega,\mathbb{R}^d)$ or $L^2(\Omega;\mathbb{R}^{d\times d})$ by $(\cdot,\cdot)$ and the L^2 scalar product over a boundary by $\langle\cdot,\cdot\rangle$.

2.1. *Model in strong form*

In this section, the strong form of the governing model is formulated.

2.1.1. *Parameters and constitutive laws*

Let $\alpha \in \mathbb{R}$ be related to the coefficient of volume expansion, $g : \Omega \to \mathbb{R}^d$ be the external forces (for instance gravity) of the flow, $f : \Omega \to [0, \infty)$ be a heat source, and $k : \mathbb{R} \to (0, \infty)$ be the thermal conductivity. Moreover, let the Cauchy stress tensor be given by

$$\sigma := \sigma(v, p, \vartheta) = -pI + \rho\nu(\vartheta)\left(\nabla v + \nabla v^T\right), \tag{1}$$

where I is the identity matrix and $\rho > 0$ is the density. The temperature-dependent kinematic viscosity is given by

$$\nu(\vartheta) := \nu_0 e^{\frac{E_A}{R\vartheta}}, \tag{2}$$

where $E_A > 0$ and $\nu_0 > 0$ are material constants and $R > 0$ is the universal gas constant. Specifically, (2) is the Arrhenius equation; see [33, 34] for chemical reactions and [35–39] for viscosity.

2.1.2. *Strong form*

With these definitions at hand, our problem statement reads: Find vector-valued velocities $v : \Omega \to \mathbb{R}^d$, a scalar-valued pressure $p : \Omega \to \mathbb{R}$, and a scalar-valued temperature $\vartheta : \Omega \to (0, \infty)$ such that

$$\begin{aligned} (\rho v \cdot \nabla) v - \nabla \cdot \sigma - \alpha \vartheta g &= 0 \quad \text{in} \quad \Omega, \\ \nabla \cdot v &= 0 \quad \text{in} \quad \Omega, \\ -\nabla \cdot (k(\vartheta)\nabla\vartheta) + v \cdot \nabla\vartheta &= f \quad \text{in} \quad \Omega. \end{aligned} \tag{3}$$

In the manner of the Boussinseq approximation, [40, 41], possible variations of the density due to temperature differences are neglected except for their most significant effect in the form of buoyancy forces $(-\alpha\vartheta g)$, so that in (3) ρ is constant.

2.1.3. *Boundary conditions*

Furthermore, we have fluid flow boundary conditions

$$\begin{aligned} v &= v_D \quad \text{on} \quad \Gamma_{vD}, \\ \rho\nu(\vartheta)\frac{\partial v}{\partial n} - p \cdot n &= \sigma_N \quad \text{on} \quad \Gamma_{vN}, \end{aligned} \tag{4}$$

where v_D is some given Dirichlet data and σ_N is the Neumann data. It is assumed that Γ_{vD} has a non-zero ($(d-1)$-dimensional) measure. Moreover, n denotes the outer normal vector. Next, we have the temperature boundary conditions

$$\begin{aligned} \vartheta &= \vartheta_D \quad \text{on} \quad \Gamma_{\vartheta D}, \\ k(\vartheta)\frac{\partial \vartheta}{\partial n} &= 0 \quad \text{on} \quad \Gamma_{\vartheta N}, \end{aligned}$$

with given Dirichlet data $\vartheta_D > 0$. Here, we assume that $\Gamma_{\vartheta D}$ has a non-zero measure. The different boundary parts and their values are specified for each example.

2.2. *Weak form*

In this subsection, we present the weak formulation via variational-monolithic coupling by standard arguments. First we construct the function spaces:

$$\begin{aligned}
V^v &:= \left\{ v \in \left[H^1(\Omega)\right]^d \,\middle|\, v = 0 \quad \text{on} \quad \Gamma_{vD} \right\},\\
V^p &:= L^2(\Omega)/\mathbb{R},\\
V^\vartheta &:= \left\{ \vartheta \in H^1(\Omega) \,\middle|\, \vartheta = 0 \quad \text{on} \quad \Gamma_{\vartheta D} \right\}.
\end{aligned}$$

Let us introduce the space $X := V^v \times V^p \times V^\vartheta$. In the following, we give a weak formulation using the notation of a semi-linear form $A(U)(\Psi)$ which is nonlinear in its first argument (i.e., the trial function U) and linear with respect to the second argument (i.e., the test function Ψ). This gives

Problem 1. *Let $\{\pi v_D, 0, \pi\vartheta_D\}$ be an extension of nonhomogeneous Dirichlet data. Furthermore, let the semi-linear form $A(U)(\Psi)$ be given by*

$$\begin{aligned}
A(U)(\Psi) := &\left(\rho(v\cdot\nabla)v, \psi^v\right) + \left(\sigma, \nabla\psi^v\right) - \langle \sigma_N, \psi^v\rangle_{\Gamma_{vN}} - \left(\alpha\vartheta g, \psi^v\right)\\
&+ \left(\nabla\cdot v, \psi^p\right)\\
&+ \left(k(\vartheta)\nabla\vartheta, \nabla\psi^\vartheta\right) + \left(v\cdot\nabla\vartheta, \psi^\vartheta\right) - \left(f, \psi^\vartheta\right), \qquad U \in X^D, \Psi \in X,
\end{aligned} \tag{5}$$

where σ is as in (1)*, ν is taken from* (2) *and $k\colon \mathbb{R} \to (0,\infty)$ is a continuous positive function.*

Find $U = (v, p, \vartheta) \in X^D := \{\pi v_D, 0, \pi\vartheta_D\} + X$ such that

$$A(U)(\Psi) = 0 \quad \forall\, \Psi := \left(\psi^v, \psi^p, \psi^\vartheta\right) \in X. \tag{6}$$

We recall [18, Theorem 2.1], merely adjusting the notation to the problem description given above:

Theorem 2. *Let $\Omega \subset \mathbb{R}^d$, $d \in \{2,3\}$, be a bounded domain with Lipschitz boundary, $\nu, k \in C^0(\mathbb{R})$ positive functions, assume $\alpha \in \mathbb{R}$, $g \in [L^2(\Omega)]^d$, $\vartheta_D \in H^{\frac{1}{2}}(\partial\Omega) \cap L^\infty(\partial\Omega)$. Let $f = 0$, $v_D = 0$, $\Gamma_{vD} = \partial\Omega$, $\Gamma_{vN} = \emptyset$, $\Gamma_{\vartheta D} = \partial\Omega$. and $\Gamma_{\vartheta N} = \emptyset$. Then the problem has a weak solution.*

The extension of the problem of [18] by a non-zero external source f is straight-forward. For the change of the fluid boundary conditions to the mixed conditions in (4) we refer to [42, Sec. 3], where solvability of a Navier–Stokes system with these boundary conditions, but without any influence of the temperature, was proven.

2.3. *Discretization and numerical solution*

The problem in equation (6) is discretized with a Galerkin finite element scheme [43] using quadrilaterals with hanging nodes for local mesh refinement. The choice of employing quadrilaterals is motivated by the finite element library deal.II [44, 45] that we use for the implementation and numerical simulations. To this end, we introduce finite dimensional conforming subspaces $X_h \subset X$, where $X_h = V_h^v \times V_h^p \times V_h^\vartheta$. Furthermore, let $\{\pi v_{h,D}, 0, \pi\vartheta_{h,D}\}$ be an extension of the discretized boundary data. Then, the problem statement reads: Find $U_h = (v_h, p_h, \vartheta_h) \in X_h^D = \{\pi v_{h,D}, 0, \pi\vartheta_{h,D}\} + X_h$ such that

$$A(U_h)(\Psi_h) = 0 \quad \forall\, \Psi_h \in X_h. \tag{7}$$

This finite-dimensional nonlinear system is solved with Newton's method: Given an initial guess $U_h^0 \in \{\pi v_{h,D}, 0, \pi\vartheta_{h,D}\} + X_h$, find $\delta U_h \in X_h$ for $j = 1, 2, 3, \ldots$ such that

$$A'\left(U_h^j\right)(\delta U_h, \Psi_h) = -A\left(U_h^j\right)(\Psi_h) \quad \forall\, \Psi_h \in X_h. \tag{8}$$

$$U_h^{j+1} = U_h^j + \omega\delta U_h, \tag{9}$$

where $\omega \in (0,1]$ is a line-search parameter for globalization. Inside Newton's method, the arising systems of linear equations are solved with a sparse direct solver (UMFPACK [46]).

3. Goal-oriented error control

In goal-oriented error estimation the aim is to estimate the error in a certain quantity of interest $J : X^D \mapsto \mathbb{R}$. Examples for such quantities of interest could be a point evaluation, an integral evaluation of any solution component or some other possibly nonlinear quantity J. In the following, first the abstract primal problem from before is stated, and subsequently the associated adjoint problem is given. Both are employed to derive an error identity.

3.1. *Primal problem*

The primal problem is given by: Find $U = (v, p, \vartheta) \in X^D$ such that

$$A(U)(\Psi) = 0 \quad \forall\, \Psi \in X. \tag{10}$$

The discrete version of this problem reads as discussed above: Find $U_h = (v_h, p_h, \vartheta_h) \in X_h^D$, such that

$$A(U_h)(\Psi_h) = 0 \quad \forall\, \Psi_h \in X_h.$$

Our aim is to obtain $J(U)$, however all we can compute is $J(U_h)$. To estimate the error we use the adjoint problem for J as proposed in [25, 47]. This approach is known as dual-weighted residual method (DWR), which is inspired by optimal control, and therefore both are conceptionally similar. In the DWR method we aim to minimize the approximation error subject to a PDE constraint, here $A(U)(\Psi) = 0$. The approximation error may consist of the discretization error only, but can also include iteration errors [29, 48, 49] or model errors [27, 28]. This minimization problem is given by [25, Section 2.2]

$$\min J(U) \quad \text{s.t.} \quad A(U)(\Psi) = 0,$$

which can be solved by formulating the Lagrangian $L(U, Z)$ with the adjoint variable $Z \in X$. The resulting optimality system is obtained by differentiation with respect to U and Z, which is conceptionally similar to numerical optimization such as optimal control or topology optimization [50–53].

3.2. *Adjoint problem*

The adjoint problem is given by: Find $Z = (z^v, z^p, z^\vartheta) \in X$ such that

$$A'(U)(\Psi, Z) = J'(U)(\Psi) \quad \forall\, \Psi \in X, \tag{11}$$

where A' and J' are the Fréchet derivatives with respect to U. However, also the adjoint problem has to be discretized. The discretized adjoint problem reads: Find $Z_h = (z_h^v, z_h^p, z_h^\vartheta) \in X_h$ such that

$$A'(U_h)(\Psi_h, Z_h) = J'(U_h)(\Psi_h) \quad \forall\, \Psi_h \in X_h. \tag{12}$$

3.3. *Error representation*

Using the solutions of the primal and adjoint problem, we obtain the following theorem:

Theorem 3. *Let A be as in* (5) *and $J \in \mathscr{C}^3(X^D,\mathbb{R})$. If U solves* (10) *and Z solves* (11) *for U, then for every $\widetilde{U} \in X^D$ and $\widetilde{Z} \in X$, the error $J(U) - J(\widetilde{U})$ can be written as*

$$J(U) - J(\widetilde{U}) = \frac{1}{2}\rho(\widetilde{U})(Z - \widetilde{Z}) + \frac{1}{2}\rho^*(\widetilde{U},\widetilde{Z})(U - \widetilde{U}) - \rho(\widetilde{U})(\widetilde{Z}) + \mathscr{R}^{(3)}\left(\widetilde{U},\widetilde{Z},e_u,e_z\right), \tag{13}$$

where the primal and adjoint residuals are given by

$$\rho(\widetilde{U})(\cdot) := -A(\widetilde{U})(\cdot),$$
$$\rho^*(\widetilde{U},\widetilde{Z})(\cdot) := J'(\widetilde{U}) - A'(\widetilde{U})(\cdot,\widetilde{Z}),$$

respectively, and the remainder term

$$\mathscr{R}^{(3)}\left(\widetilde{U},\widetilde{Z},e_u,e_z\right) := \frac{1}{2}\int_0^1 \Big[J'''\left(\widetilde{U} + se_u\right)(e_u,e_u,e_u) - A'''\left(\widetilde{U} + se_u\right)\left(e_u,e_u,e_u,\widetilde{Z} + se_z\right) - 3A''\left(\widetilde{U} + se_u\right)(e_u,e_u,e_u)\Big] s(s-1)\,ds, \tag{14}$$

with $e_u = U - \widetilde{U}$ and $e_z = Z - \widetilde{Z}$.

This error representation allows us to represent the error in a different way. However (13) still depends on U and Z, which are both unknown.

Proof. For information on the proof, we refer to [25, 29, 32]. Note that we use positivity of ϑ in order to avoid singularities in ρ, ρ^* and $\mathscr{R}^{(3)}$. □

Remark 4. Since this error representation holds for all $\widetilde{U}$ and $\widetilde{Z}$, it also holds for $\widetilde{U} = U_h$ and $\widetilde{Z} = Z_h$, provided that $U_h \in X^D$ and $Z_h \in X$. We note that $X_h \subset X$, but for non-trivial boundary data, $X_h^D \not\subset X^D$.

3.4. *Error estimators*

If we replace U and Z in (13) by approximations, we obtain an error estimator instead of an error representation. This can be realized by higher order interpolation or enriched approximation. Both methods are described in more details in [25] and a mixed method is presented in [23,30]. In this work, we will use and describe enriched approximation in more detail. We consider $X_h^{(2)}$ and $X_h^{0,(2)}$ to be enriched spaces, i.e $X_h \subset X_h^{(2)} \subset X$ and $X_h^0 \subset X_h^{0,(2)} \subset X^0$. Examples of such enriched spaces can be generated by refining the mesh or using other finite elements. This leads us to the enriched model problem: Find $U_h^{(2)} = (v_h^{(2)}, p_h^{(2)}, \vartheta_h^{(2)}) \in X_h^{(2)}$, such that

$$A\left(U_h^{(2)}\right)\left(\Psi_h^{(2)}\right) = 0 \quad \forall\, \Psi_h^{(2)} \in X_h^{0,(2)}. \tag{15}$$

The enriched adjoint problem reads: Find $Z_h^{(2)} = (z_h^{v,(2)}, z_h^{p,(2)}, z_h^{\vartheta,(2)}) \in X_h^{0,(2)}$ such that

$$A'\left(U_h^{(2)}\right)\left(\Psi_h^{(2)}, Z_h^{(2)}\right) = J'\left(U_h^{(2)}\right)\left(\Psi_h^{(2)}\right) \quad \forall\, \Psi_h^{(2)} \in X_h^{0,(2)}. \tag{16}$$

As above, U and Z in the right hand side of the error representation (13) are replaced by $U_h^{(2)}$ and $Z_h^{(2)}$ and $\widetilde{U}$ and $\widetilde{Z}$ by U_h and Z_h, respectively. We obtain the error estimation formula

$$J(U) - J(U_h) \approx \underbrace{\frac{1}{2}\rho(U_h)\left(Z_h^{(2)} - Z_h\right) + \frac{1}{2}\rho^*(U_h,Z_h)\left(U_h^{(2)} - U_h\right)}_{\eta_h} \underbrace{-\rho(U_h)(Z_h)}_{\eta_k} + \underbrace{\mathscr{R}^{(3)}\left(U_h,Z_h,e_u^{(2)},e_z^{(2)}\right)}_{\eta_{\mathscr{R}}}, \tag{17}$$

where $e_u^{(2)} := U_h^{(2)} - U_h$ and $Z_h^{(2)} - Z_h$. Here $U_h^{(2)}$ and $Z_h^{(2)}$ are the solutions of (15) and (16) respectively.

Remark 5. For the error estimator (17), U_h and Z_h need not be the exact solutions of the discrete problem but can be some approximations of it as well.

The first part of the error estimator η_h

The part η_h represents the discretization error as proposed in [22,29,32]. Here

$$\eta_{h,p} := \rho(U_h)\left(Z_h^{(2)} - Z_h\right)$$

is the primal part of the error estimator and

$$\eta_{h,a} := \rho^*(U_h, Z_h)\left(U_h^{(2)} - U_h\right)$$

is the adjoint part. In the literature the adjoint part of the error estimator is often replaced with the primal error part ρ. In [25,54], it is proven that the adjoint part can be expressed as the primal part and higher order terms depending on the problem and the goal functionals. For moderate nonlinear problems, this approximation often works very well [25,55]. In this work, both parts are considered. The localization is done by using the partition of unity technique proposed in [31]. Alternatives are the filtering approach [28] (which works as well on the variational level) or integration by parts [25]. However, specifically for coupled problems (as in the current work) the latter is error prone and computationally expensive since the strong form operators must be evaluated.

The second part of the error estimator η_k

This part mimics the iteration error as in [29,32]. It can be used as stopping criterion of the solver on each level. If U_h is the exact solution of (7) then this part vanishes.

The third part of the error estimator $\eta_{\mathscr{R}}$

This part is usually of higher order [25,29]. Mostly, $\eta_{\mathscr{R}}$ is neglected in the evaluation of the error estimator. Recent studies and investigations of $\eta_{\mathscr{R}}$ with the help of numerical examples were undertaken in [32].

The practical error estimator

After the previous assumptions and explanations, the practical error estimator is given by $\eta := \eta_h + \eta_k$. As proven in [32] (see also [22]), this error estimator is efficient and reliable if a certain saturation assumption is fulfilled. Furthermore, interpolation techniques for a new class of algorithms were established in [30].

3.5. *Finite element discretization and polynomial spaces*

Having the primal and adjoint problems at hand, we employ the following finite elements in our algorithms and numerical experiments. We use

- continuous piecewise bi-quadratic functions Q_2^c for the velocity v and
- continuous piecewise bilinear functions Q_1^c for the pressure p and temperature ϑ.

The adaptively refined mesh will lead to hanging nodes in the mesh [56]. These nodes are constrained such that generated functions in the finite element space are continuous. For more information about this topic we refer to [57,58]. For the enriched space we have

- continuous piecewise bi-quartic functions Q_4^c for the velocity v and
- continuous piecewise quadratic functions Q_2^c for the pressure p and temperature ϑ.

A comparison of different finite elements and uniform mesh refinement for the enriched space can be found in [59].

3.6. *Multiple goal functionals and algorithms*

In many applications, such as multiphysics problems, or coupled problems in general (as in this work), more than one goal functional is of interest. Let us assume we are interested in N goal functionals $J_1, \dots, J_N$. Later in Section 4, we have up to $N = 7$. A straightforward application of the previous concepts would be to compute an error estimator for each functional and to combine them afterwards. However, for this approach we have to solve the adjoint problem N times; see [19, 60]. This would lead to a non-acceptable computational cost. To overcome this problem, several techniques have been proposed such as a combined functional by solving an additional dual-dual problem for the sign computation in the combined functional [19, 60], using generalized Green's functions [61], by a linear combination of the functionals [62, 63], by reformulation to a minimization problem where the quantities of interest serve as constraints [64, 65], and combined functionals with hierarchical higher order approximations for the sign computation [20, 22, 66]. In this work we follow the approach proposed in [20, 66]. We combine the functionals to one by using

$$J_c := \sum_{i=1}^{N} \omega_i J_i, \tag{18}$$

with

$$\omega_i := \begin{cases} \operatorname{sign}\left(J_i\left(U_h^{(2)}\right) - J_i(U_h)\right) / |J_i(U_h)| & \text{for } |J_i(U_h)| \geq 10^{-12}, \\ 10^3 \operatorname{sign}\left(J_i\left(U_h^{(2)}\right) - J_i(U_h)\right). \end{cases}$$

The overall algorithmic realization using J_c has been described in detail in [32] and we simply apply exactly these schemes to the Boussinesq model in the current paper.

4. Numerical experiments

In this section, we investigate three numerical examples. The programming code is based on the open-source finite element library deal.II [44, 45]. All geometry data and material parameters are given in SI units. To measure the quality of our error estimators we employ so-called effectivity indices.

Definition 6. *For the functional J the effictivity index I_{eff}, the primal effectivity index $I_{eff,p}$ and the adjoint effectivity index $I_{eff,a}$ are defined as*

$$I_{eff} := \frac{\eta_h}{J(U) - J(U_h)}, \qquad I_{eff,p} := \frac{\eta_{h,p}}{J(U) - J(U_h)} \quad \text{and} \quad I_{eff,a} := \frac{\eta_{h,a}}{J(U) - J(U_h)}.$$

For the real error $J(U) - J(U_h)$, we compute a reference solution on sufficiently refined meshes as it is often done.

4.1. *A flow benchmark*

In this first example we apply our method to a problem featuring a flow around a cylinder as in [67].

4.1.1. *Configuration, geometry, parameters, boundary conditions*

The domain is given by $\Omega := (0, 2.2) \times (0, 0.41) \setminus \mathscr{B}$ where $\mathscr{B} := \{x \in \mathbb{R}^2 : |x - (0.2, 0.2)| < 0.05\}$. The domain as well as the boundary conditions are depicted in Figure 1.

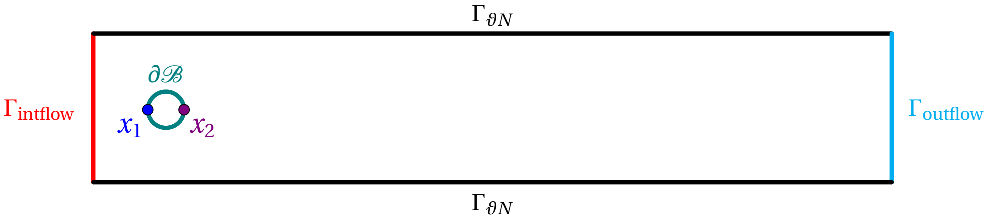

Figure 1. The domain Ω with boundary conditions.

In the strong model given in Section 2.1, we set $g = (0,0)^T, k(\vartheta) = 1$ and[1] $E_A = 1.49 \times 10^4$, $v_0 = 2.22 \times 10^{-6}$, and $R = 8.31$. Next, the thermal expansion coefficient is $\alpha = 6.88 \times 10^{-5}$ and the density is $\rho = 998.21$. Constant conductivity was chosen for simplicity, in order to focus on prototype situations within the development of the multigoal framework for the Boussinesq model.

Furthermore we have no-slip boundary conditions on $\Gamma_{\vartheta N}$ and $\partial\mathscr{B}$, do-nothing conditions on Γ_{outflow} and an inflow on Γ_{intflow}, i.e

$$\begin{aligned} v = 0 \quad &\text{on} \quad \Gamma_{\vartheta N} \cup \partial\mathscr{B}, \\ v = v_{in} \quad &\text{on} \quad \Gamma_{\text{intflow}}, \\ \sigma \cdot n = 0 \quad &\text{on} \quad \Gamma_{\text{outflow}}, \\ \frac{\partial\vartheta}{\partial n} = 0 \quad &\text{on} \quad \partial\Omega \setminus (\partial\mathscr{B} \cup \Gamma_{\text{intflow}}), \\ \vartheta = \vartheta_{\text{intflow}} \quad &\text{on} \quad \Gamma_{\text{intflow}}, \\ \vartheta = \vartheta_{\partial\mathscr{B}} \quad &\text{on} \quad \partial\mathscr{B}, \end{aligned}$$

where $v_{in}(x,y) := 4 v_m \frac{y(H-y)}{H^2}$ with $v_m = 0.3$ and $H = 0.41$. In the following, two possible configurations are considered:

- “cold to warm”: $\vartheta_{\text{intflow}} = 278.15$, $\vartheta_{\partial\mathscr{B}} = 353.15$,
- “warm to cold”: $\vartheta_{\text{intflow}} = 353.15$, $\vartheta_{\partial\mathscr{B}} = 278.15$.

4.1.2. *Goal functionals*

In this example, a pressure difference serves as goal functional:

$$p_{\text{diff}}(U) := p\,(x_1) - p(x_2),$$

where $x_1 := (0.15, 0.2)$ and $x_2 := (0.25, 0.2)$ as in the original benchmark problem [67]. The reference values are

$$p_{\text{diff}}(U) = 114.68898895581040 \quad \text{for “cold to warm”}$$

and

$$p_{\text{diff}}(U) = 101.97737719601436 \quad \text{for “warm to cold”.}$$

We remark that due to the pointwise evaluation $p_{\text{diff}}(U)$ is not well-defined on the solution space X^D introduced in Section 2.2 and the adjoint equation features Dirac delta distributions at x_1 and

---

[1] The values are computed by using the data for 293.15K and 353.15K in https://www.lss.ovgu.de/lss_media/Downloads/Lehre/Str%C3%B6mungsmechanik/Arbeitsheft/IV.pdf.

x_2 on the right hand side. Therefore higher regularity of solutions to (6) (respectively (3)) has to be assumed here. For corresponding conditions on data and domain cf. also [18, Theorem 2.3].

4.1.3. *Discussion of our findings*

The numerical results are displayed in Figures 2 to 7. More precisely, Figure 2 and Figure 3 show the error and error estimator for the configurations “cold to warm” and “warm to cold”, respectively. The magnitude of the velocity (including streamlines), the pressure and the temperature are visualized in the next three figures for both configurations. Finally, the meshes are displayed in Figure 7.

We observe that in the configuration “cold to warm” the vortices are much bigger than in the configuration “warm to cold”. This is a result of the temperature dependent viscosity, which is smaller around the cold cylinder. This also leads to higher convection terms in the configuration “cold to warm”. In Figure 7, we notice that this effect also has a big influence in the adaptive refinement. In both configurations the temperature is almost constant on the other side of the cylinder, see Figure 6. Furthermore, it is close to the temperature at $\partial\mathcal{B}$. From Figure 5, we deduce that the high dependency of the viscosity on the temperature has a big impact on the pressure p. The error reduces approximately with the rate $\mathcal{O}(\mathrm{DOFs}^{-1})$ for both configurations, cf. Figure 2 and Figure 3, respectively. Surprisingly, the error estimator shows a more uniform behavior in the convergence than the error itself. One can observe a strong refinement of the mesh around the cylinder. On the other hand, the mesh has almost no refinement on the right side, namely on the outflow boundary.

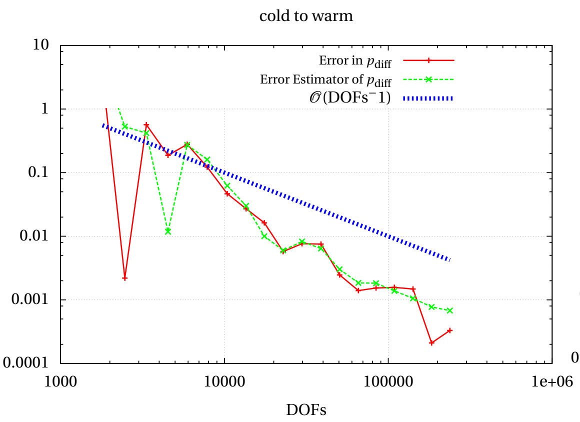

Figure 2. The error and error estimator for p_{diff} for the configuration “cold to warm”.

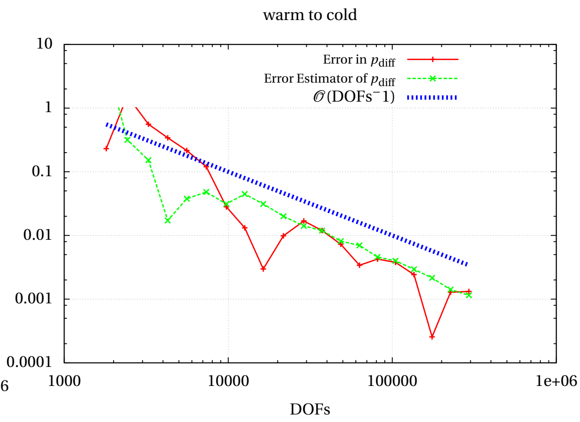

Figure 3. The error and error estimator for p_{diff} for the configuration “warm to cold”.

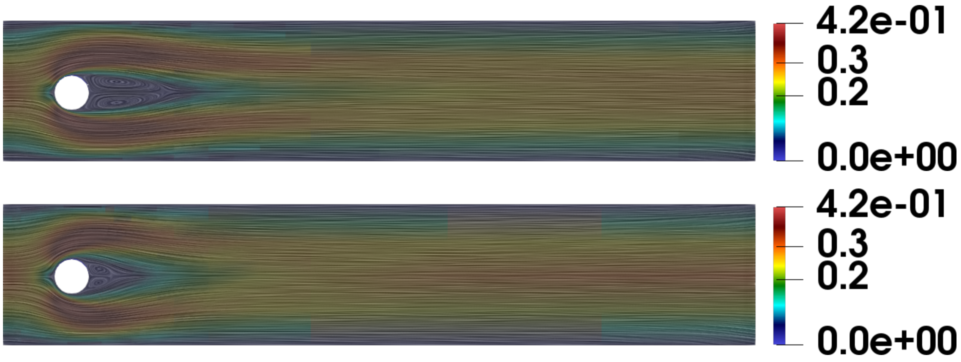

Figure 4. The magnitude of the velocity and the streamlines for “cold to warm” (above) and “warm to cold” (below)

Figure 5. The pressure p for the configuration “cold to warm” (above) and “warm to cold” (below)

Figure 6. The temperature ϑ for the configuration “cold to warm” (above) and “warm to cold” (below)

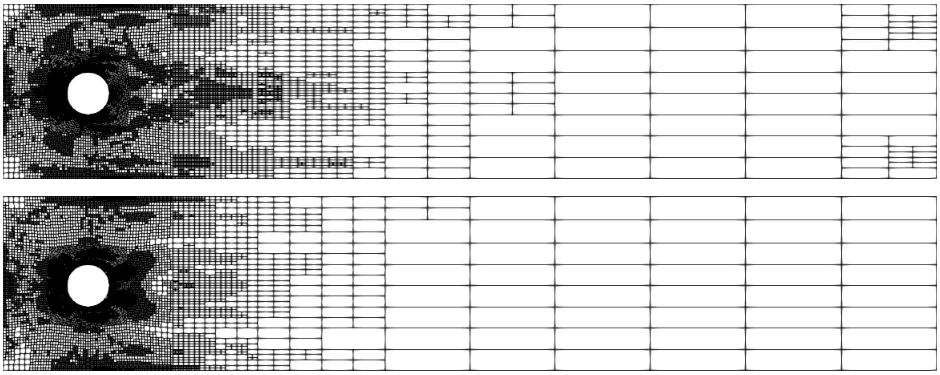

Figure 7. The mesh for the configuration “cold to warm” (above) and “warm to cold” (below)

4.2. *Laser point source*

In this second example, we consider the flow in a square without inflow and outflow. The temperature on the boundary is constant. A heat point source[2] enters as right hand side into the flow equations and generates a flow field.

4.2.1. *Configuration, geometry, parameters, boundary conditions*

We consider $\Omega := (0,1)^2$. The right hand side f of (3) is

$$f(x) := 10\psi_{x_0}(x) \quad \text{where} \quad \psi_{x_0}(x) := 10^4\sqrt{2\pi}e^{-10^4|x-x_0|^2},$$

with $x_0 := (0.75, 0.75)$. This models a laser pointing at x_0. The boundary conditions are

$$v = 0 \text{ on } \partial\Omega \quad \text{and} \quad \vartheta = 293.15 \text{ on } \partial\Omega.$$

The gravity is given by $g = (0, -9.81)^T$ and the thermal expansion coefficient is $\alpha = 6.88 \times 10^{-5}$.

4.2.2. *Goal functionals*

Our quantities of interest are the mean value of the velocity and the mean value of the temperature

$$|\bar{v}|(U) := \frac{1}{|\Omega|}\int_\Omega |v|\mathrm{d}x \qquad \text{and} \qquad \bar{\vartheta}(U) := \frac{1}{|\Omega|}\int_\Omega \vartheta\mathrm{d}x.$$

We use the adaptive strategy for $|\bar{v}|$, $\bar{\vartheta}$, and for both of these at once in the combined functional $J_{\mathfrak{C}}$.

4.2.3. *Discussion of our findings*

The numerical results are presented in Figures 8 to 16. More precisely, the first six figures display error and error estimator in one picture and effectivity index in a second picture for the temperature $\bar{\vartheta}$, the absolute value of the velocity $|\bar{v}|$ and the combination of both, respectively. The streamlines of the flow and the magnitude of the temperature ϑ are displayed in Figure 14 left. The refined meshes after 21 refinement steps are depicted in Figure 15. In Figure 16, the value of the error estimator and the marked elements are displayed. Good effectivity indices for $|\bar{v}|$, $\bar{\vartheta}$ and for the combination $J_{\mathfrak{C}}$ are observed on the refined meshes. Figure 12 provides us information on the error of the individual functionals, the combined error and the error estimator. The error for

---

[2] The motivation of this example is due to laser wave guide modeling in which a laser causes temperature changes and for which material starts to flow.

$|\bar{v}|$ dominates the error of $\bar{\vartheta}$. Therefore, $J_{\mathfrak{C}}$ has a similar behavior as $|\bar{v}|$. This is an explanation for the similar behaviour of the refined meshes. In all three cases, there is a strong refinement around the point source. This clover is a typical refinement structure around point sources. There is a big vortex in the center, two smaller vortices on the right side, c.f. Figure 14. Moreover, there are smaller vortices in the left vertices of the square. This is similar to the driven cavity problem. A more detailed picture of this part of the domain is displayed in Figure 14 (right).

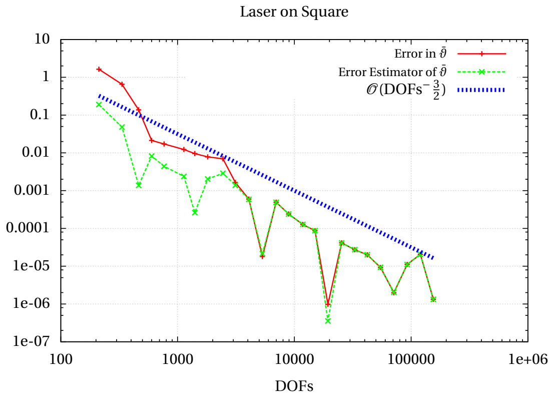

Figure 8. The error and error estimator for $\bar{\vartheta}$.

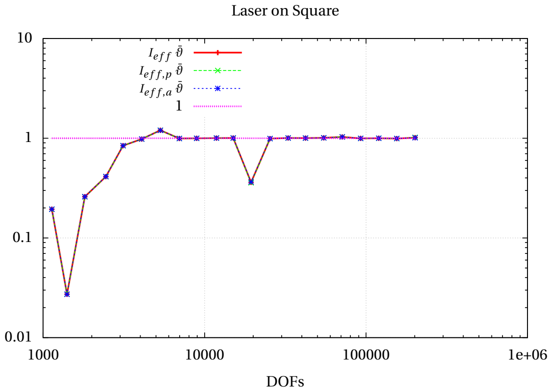

Figure 9. The effectivity indices for $\bar{\vartheta}$.

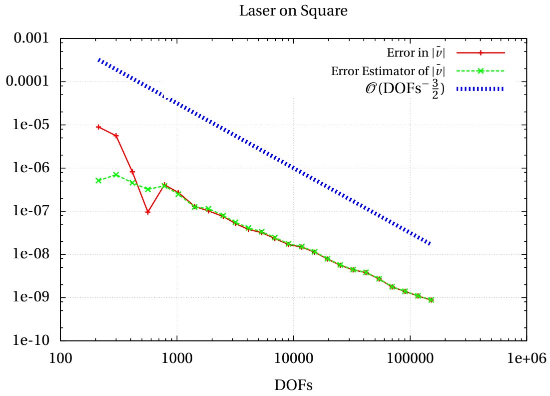

Figure 10. The error and error estimator for $|\bar{v}|$.

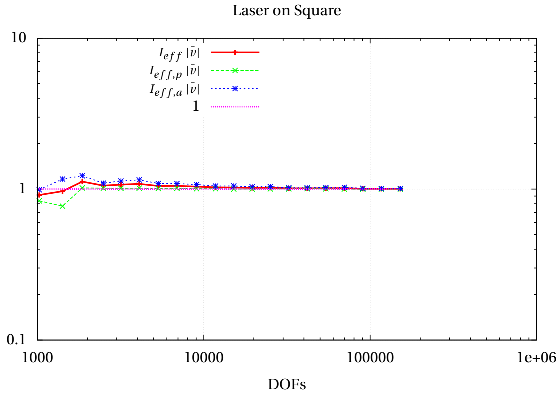

Figure 11. The effectivity indices for $|\bar{v}|$.

4.3. *Y-beam splitter*

In this third example, we consider a Y-beam splitter with a laser that generates a flow field due to gravity. This application is motivated from PhoenixD[3] and is an important configuration in wave guide modeling [68].

---

[3] https://www.phoenixd.uni-hannover.de/en/

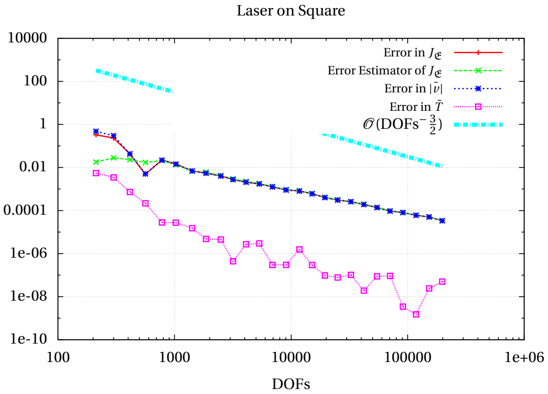

Figure 12. The error and error estimator for $J_{\mathfrak{E}}$ for $|\bar{v}|$ and $\bar{T}$.

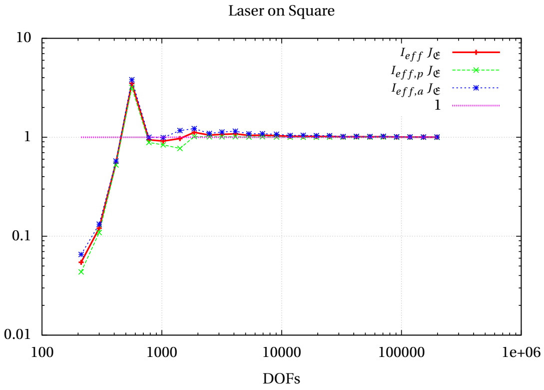

Figure 13. The effectivity indices for $J_{\mathfrak{E}}$ for $|\bar{v}|$ and $\bar{T}$.

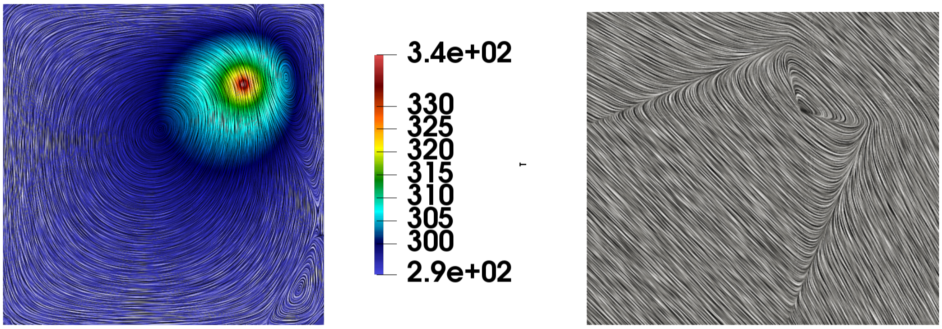

Figure 14. Section 4.2. Velocity streamlines and temperature (left) and zoom into the small vortex at left bottom corner (right).

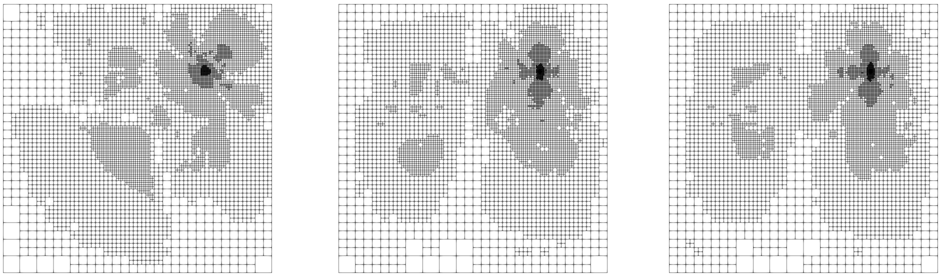

Figure 15. Section 4.2. The mesh after 21 refinements for $\bar{\vartheta}$ (left), $J_{\mathfrak{E}}$ (center) and $|\bar{v}|$(right).

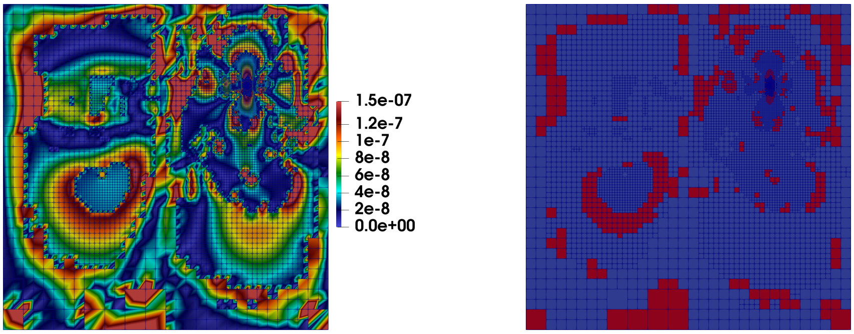

Figure 16. Section 4.2. Error estimator (left) and marked elements for refinement (right) for the mesh $J_{\mathfrak{C}}$ displayed at the center of Figure 15.

4.3.1. *Configuration, geometry, parameters, boundary conditions*

The domain Ω and its subdomains $\Omega_1, \Omega_2, \Omega_3$ are depicted in Figure 17. Furthermore, we have the fluid flow boundary conditions

$$\begin{aligned} v &= 0 \quad &\text{on} \quad && \Gamma_0 = \Gamma_{vD}, \\ \nu(\vartheta)\frac{\partial v}{\partial n} - p \cdot n &= 0 \quad &\text{on} \quad && \Gamma_1 \cup \Gamma_2 \cup \Gamma_3 = \Gamma_{vN}, \end{aligned}$$

the temperature boundary conditions

$$\begin{aligned} \vartheta &= 293.15 \quad &\text{on} \quad && \Gamma_1 = \Gamma_{\vartheta D}, \\ \frac{\partial \vartheta}{\partial n} &= 0 \quad &\text{on} \quad && \partial\Omega \setminus \Gamma_1 = \Gamma_{\vartheta N}. \end{aligned}$$

The right hand side f is chosen as

- Configuration 1: $f(x) := \psi_A(x)$, $A = (0.5, 0.1)$,
- Configuration 2: $f(x) := \frac{1}{2}\psi_B(x) + \frac{1}{2}\psi_C(x)$, $B = (0.5, 0.3)$, $C = (0.5, 0.7)$,
- Configuration 3: $f(x) := \psi_E(x)$, $E = (0.5, 1)$,
- Configuration 4: $f(x) := \psi_D(x)$, $D = (0.55, 1)$,
- Configuration 5: $f(x) := \psi_F(x)$, $F = (0.3, 1.4)$,
- Configuration 6: $f(x) := \psi_{\mathfrak{C}}(x)$.

The function

$$\psi_{x_0}(x) := 10^4\sqrt{2\pi}e^{-10^4|x-x_0|^2},$$

resembles the laser centered at $x_0 \in \{A, B, C, D, E, F\}$, and the function

$$\psi_{\mathfrak{C}}(x) := \frac{500}{|\mathfrak{C}|}\sqrt{2\pi}e^{-10^4 dist(x,\mathfrak{C})^2},$$

resembles the laser along the curve $\mathfrak{C}$ where $dist(x, \mathfrak{C}) := \inf_{x^* \in \mathfrak{C}} |x - x^*|$ and $|\mathfrak{C}|$ is the length of the curve $\mathfrak{C}$. The curve $\mathfrak{C}$ is given by circular arcs, with continuous tangent through the points $((0.5, 0), A, B, C, D, E, (0.45, 1), F, (0.3, 1.5))$, where we start with a line between $(0.5, 0)$ and A.

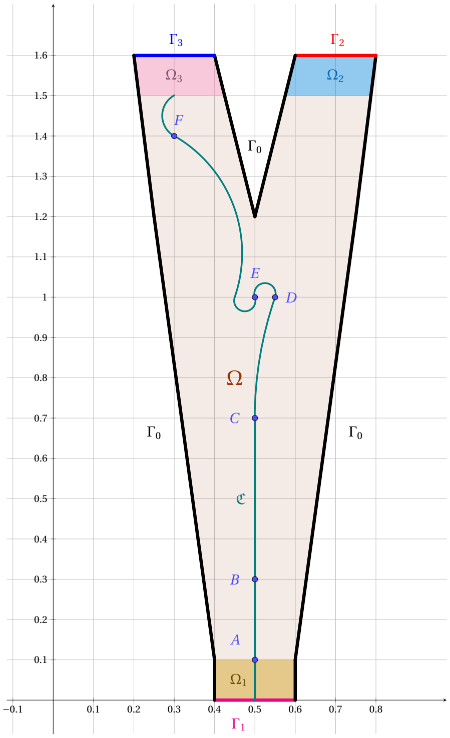

Figure 17. The domain Ω, the boundary parts, the domains for our quantites of interest, the curve ℭ and the points for the different configurations.

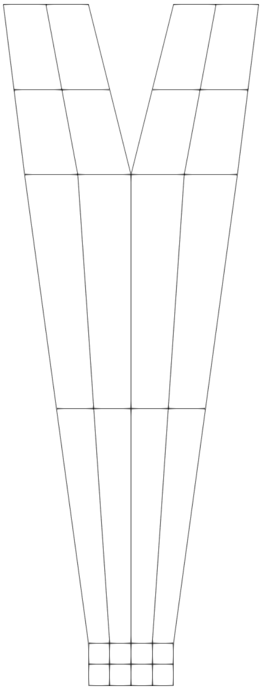

Figure 18. The initial mesh for all configurations.

4.3.2. *Goal functionals*

We consider seven goal functionals:

$$
\begin{aligned}
J_1(U) &:= \int_{\Gamma_1} v \cdot n \mathrm{d}x, & J_2(U) &:= \int_{\Gamma_2} v \cdot n \mathrm{d}x, \\
J_3(U) &:= \int_{\Gamma_3} v \cdot n \mathrm{d}x, & J_4(U) &:= \frac{1}{|\Omega_1|} \int_{\Omega_1} \vartheta \mathrm{d}x, \\
J_5(U) &:= \frac{1}{|\Omega_2|} \int_{\Omega_2} \vartheta \mathrm{d}x, & J_6(U) &:= \frac{1}{|\Omega_3|} \int_{\Omega_3} \vartheta \mathrm{d}x, \\
J_7(U) &:= (J_5(U) - J_6(U))^2.
\end{aligned}
$$

Remark 7. Due to symmetry, J_7 vanishes for the Configurations 1-3.

4.3.3. *Discussion of our findings*

The magnitude of the velocity and the temperature for different configurations are displayed in Figure 19. Furthermore, different locally refined meshes are shown in Figure 20. These show refinement in geometric singularities such as the kink where the splitter branches, but as well local refinement due to the goal functionals.

In the following, we discuss our quantitative findings. First, the reference values are provided in Table 1. The errors and error estimators versus the degrees of freedom are displayed in the Figures 21 to 26. The various effectivity indices are shown in the Figures 27 to 32, from which we observe excellent performances. This is in particular remarkable due to the different configurations and the nonlinear behavior of the coupled PDE system. It can be inferred that our multigoal framework is robust and yields a cost-efficient numerical procedure.

Table 1. Reference values

Config.	1	2	3
J_1	-5.1630481e-06	-2.1224898e-05	-3.36248616e-05
J_2	2.5815241e-06	1.0612449e-05	1.68124308e-05
J_3	2.5815241e-06	1.0612449e-05	1.68124308e-05
J_4	2.9511378e+02	2.9511878e+02	2.95118918e+02
J_5	2.9704640e+02	3.0918292e+02	3.20253892e+02
J_6	2.9704640e+02	3.0918292+02	3.20253892e+02
J_7	0	0	0

Config.	4	5	6
J_1	-3.3629129e-05	-3.7522141e-05	-7.2595565e-05
J_2	1.7183604e-05	1.3366980e-05	3.2117505e-05
J_3	1.6445525e-05	2.4155161e-05	4.0478060e-05
J_4	2.9511892e+02	2.9511902e+02	2.9670043e+02
J_5	3.2052058e+02	3.2170400e+02	3.4082013e+02
J_6	3.2001790e+02	3.3282825e+02	3.4671220e+02
J_7	2.5268810e-01	1.237489e+02	3.4716466e+01

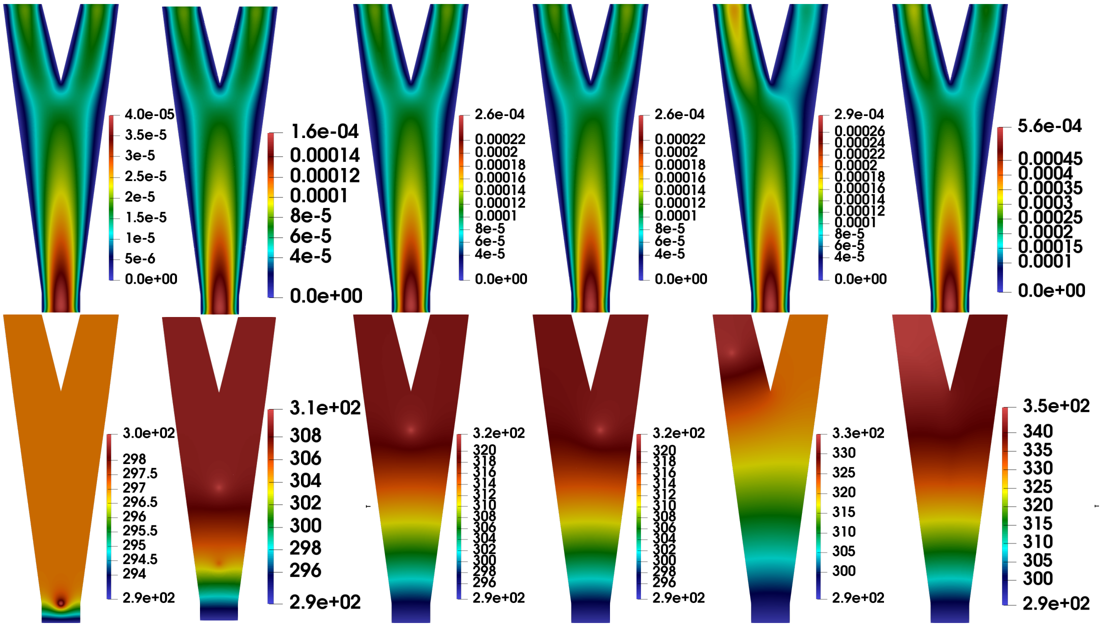

Figure 19. The magnitude of the velocity (above) and the temperature (below) for Configuration 1-6 from left to right.

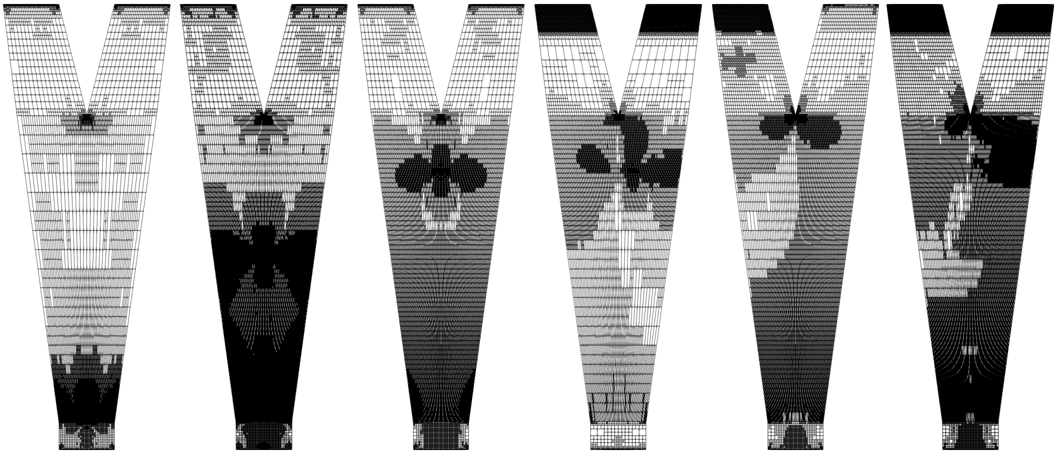

Figure 20. The initial and final mesh for Configuration 1-6 from left to right.

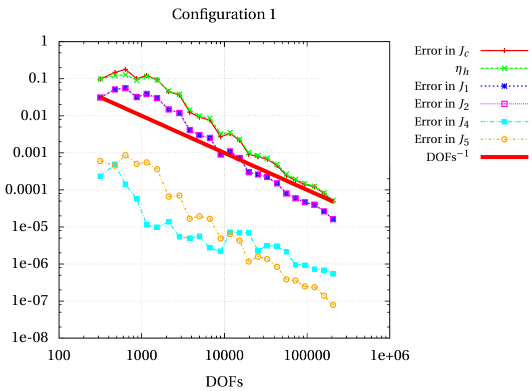

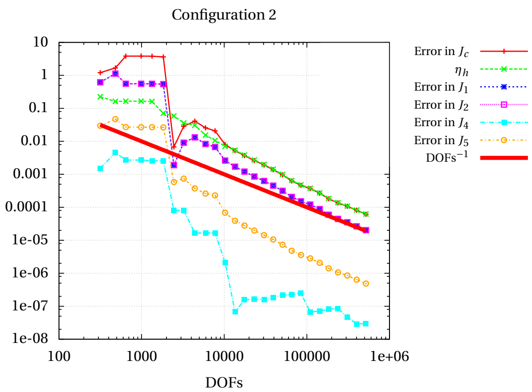

Figure 21. The error and error estimator for Configuration 1.

Figure 22. The error and error estimator for Configuration 2.

5. Conclusions

In this work, we modeled laser material processing with the help of a generalized Boussinesq model. The resulting PDE system is nonlinear and we considered a monolithic coupling scheme. The focus was on multi-goal a posteriori error estimation and local mesh adaptivity. Since the Boussinesq system consists of two coupled PDEs (i.e., incompressible Navier–Stokes coupled to a stationary heat equation) several quantities of interest (i.e., goal functionals) might be of interest simultaneously. In our multigoal-framework, a combined goal functional is defined and serves as right hand side in the adjoint problem from which local sensitivity measures enter the error estimator. Three numerical experiments were conducted: One classical benchmark problem and two configurations that are motivated from interdisciplinary collaborations in our Cluster of Excellence. In all tests, we observed error reductions and effectivity indices. The latter show excellent performance and indicate that we have a robust and efficient adaptive framework at hand. In future work, we plan to extend this framework to three-dimensional situations.

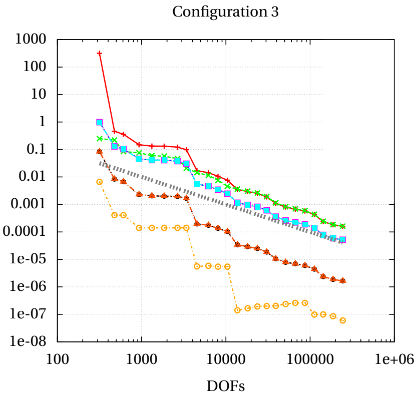

Figure 23. The errors and error estimator for Configuration 3.

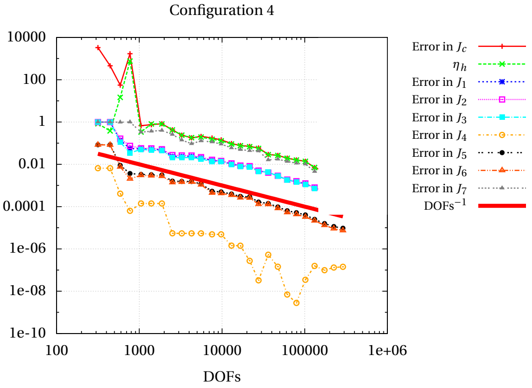

Figure 24. The errors and error estimator for Configuration 4.

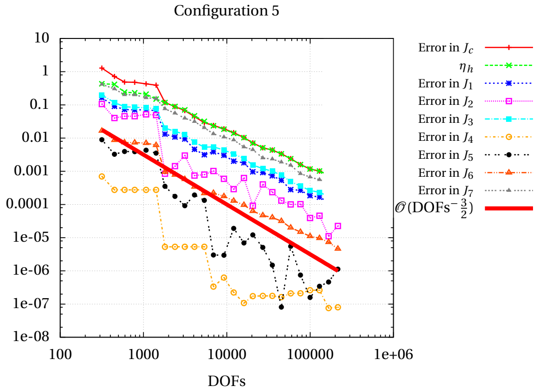

Figure 25. The errors and error estimator for Configuration 5.

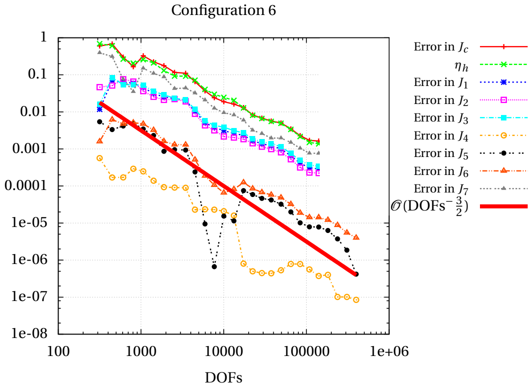

Figure 26. The errors and error estimator for Configuration 6.

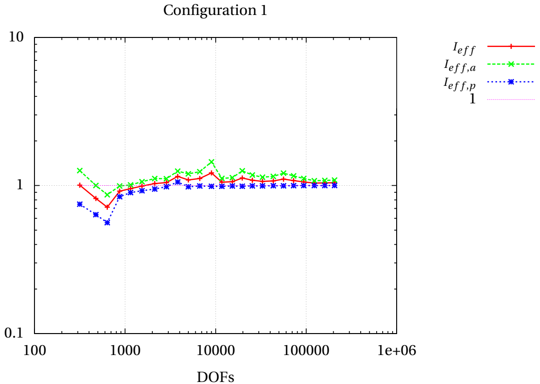

Figure 27. Effectivity indices for Configuration 1.

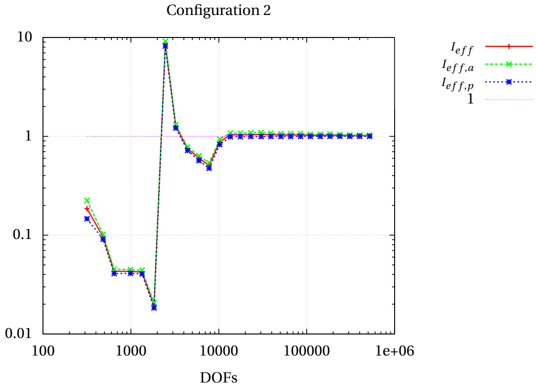

Figure 28. Effectivity indices for Configuration 2.

Theorem 2.2 and the multigoal framework in general cover three-dimensional domains (see also [22, 69]). A suitable analogue for the Y-beam splitter of Section 4.3 would be $\Omega \times I$, with $I = (0, 0.2)$, $\Gamma_{\nu N} = (\Gamma_1 \cup \Gamma_2 \cup \Gamma_3) \times I$ etc. (where Ω, Γ_1, Γ_2, Γ_3 are as in section 4.3), and the points

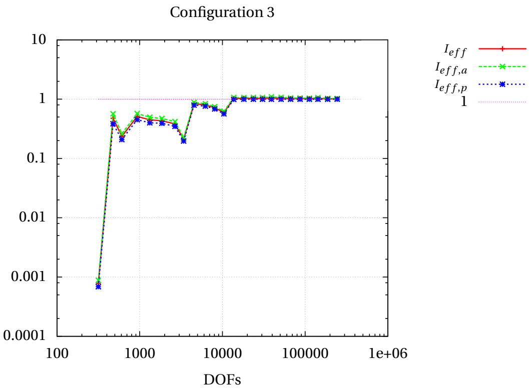

Figure 29. Effectivity indices for Configuration 3.

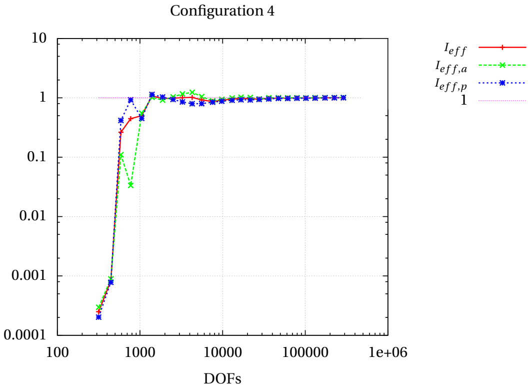

Figure 30. Effectivity indices for Configuration 4.

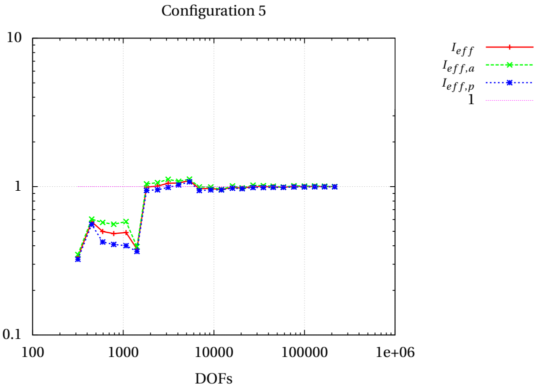

Figure 31. Effectivity indices for Configuration 5.

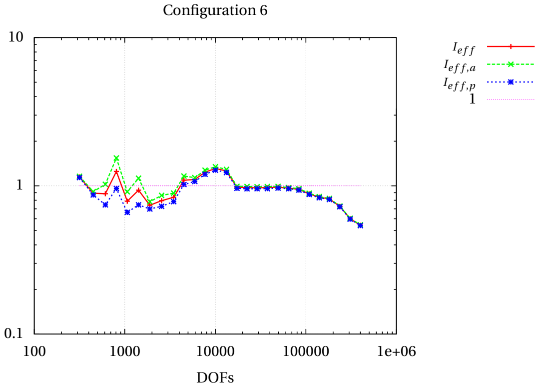

Figure 32. Effectivity indices for Configuration 6

$A,\ldots,F$ obtaining an additional third component of 0.1 each; a choice of $g = (0,0,-9.81)^T$ in place of $g = (0,-9.81)^T$ would be interesting. The form of the goal functionals of Section 4.3.2 remains unchanged. However, the computational extension requires some work, with the main bottleneck being the linear solver and preconditioners that need to be developed due to memory consumptions and computational cost. Finally, another future extension are time-dependent cases by using a space-time framework.

Conflicts of interest

The authors have no conflict of interest to declare.

References

[1] R. Temam, *Navier-Stokes Equations: Theory and Numerical Analysis*, AMS Chelsea Publication, vol. 343, American Mathematical Society, 2001.
[2] G. P. Galdi, *An Introduction to the Mathematical Theory of the Navier-Stokes Equations*, second ed., Springer, 2011.
[3] V. Girault, P.-A. Raviart, *Finite Element method for the Navier-Stokes equations*, Computer Series in Computational Mathematics, vol. 5, Springer, 1986.

[4] R. Glowinski, P. Le Tallec, *Augmented Lagrangian and Operator-Splitting Methods in Nonlinear Mechanics*, SIAM Studies in Applied Mathematics, vol. 9, Society for Industrial and Applied Mathematics, 1989.

[5] R. Glowinski, "Finite element methods for incompressible viscous flow", in *Numerical Methods for Fluids (Part 3)*, Handbook of Numerical Analysis, vol. 9, Elsevier, 2003, p. 3-1176.

[6] R. Glowinski, J. F. Periaux, "Numerical methods for nonlinear problems in fluid dynamics", in *INRIA Conference on Supercomputing: State-of-the-Art*, Elsevier, 1987, p. 381-479.

[7] M. O. Bristeau, R. Glowinski, J. F. Periaux, "Numerical methods for the Navier–Stokes equations. Applications to the simulation of compressible and incompressible viscous flows", *Comput. Phys. Rep.* **6** (1987), p. 73-187.

[8] R. Rannacher, "Finite Element Methods for the Incompressible Navier-Stokes Equations", in *Fundamental Directions in Mathematical Fluid Mechanics* (G. P. Galdi, J. G. Heywood, R. Rannacher, eds.), Birkhäuser, 2000, p. 191-293.

[9] S. Turek, *Efficient solvers for incompressible flow problems*, Letures Notes in Computational Science and Engineering, vol. 6, Springer, 1999.

[10] S. Turek, L. Rivkind, J. Hron, R. Glowinski, "Numerical analysis of a new time-stepping θ-scheme for incompressible flow simulations", Tech. report, TU Dortmund and University of Houston, 2005, Dedicated to David Gottlieb on the occasion of his 60th anniversary.

[11] J. G. Heywood, R. Rannacher, "Finite-Element Approximation of the Nonstationary Navier-Stokes Problem Part IV: Error Analysis for Second-Order Time Discretization", *SIAM J. Numer. Anal.* **27** (1990), no. 2, p. 353-384.

[12] P. G. Drazin, W. H. Reid, *Hydrodynamic Stability*, Cambridge Monographs on Mechanics and Applied Mathematics, Cambridge University Press, 1981.

[13] D. Etling, *Theoretische Meteorologie*, Springer, 2008.

[14] M. Kronbichler, T. Heister, W. Bangerth, "High Accuracy Mantle Convection Simulation through Modern Numerical Methods", *Geophys. J. Int.* **191** (2012), p. 12-29.

[15] A. Otto, M. Schmidt, "Towards a universal numerical simulation model for laser material processing", *Physics Procedia* **5** (2010), p. 35-46, Laser Assisted Net Shape Engineering 6, Proceedings of the LANE 2010, Part 1.

[16] W. M. Pätzold, A. Demircan, U. Morgner, "Low-loss curved waveguides in polymers written with a femtosecond laser", *Opt. Express* **25** (2017), no. 1, p. 263-270.

[17] G. Y. Chen, F. Piantedosi, D. Otten, Y. Q. Kang, W. Q. Zhang, X. Zhou, T. M. Monro, D. G. Lancaster, "Femtosecond-laser-written Microstructured Waveguides in BK7 Glass", *Sci. Rep.* **8** (2018), no. 1, article no. 10377.

[18] S. A. Lorca, J. L. Boldrini, "Stationary Solutions for Generalized Boussinesq Models", *J. Differ. Equations* **124** (1996), no. 2, p. 389-406.

[19] R. Hartmann, "Multitarget error estimation and adaptivity in aerodynamic flow simulations", *SIAM J. Sci. Comput.* **31** (2008), no. 1, p. 708-731.

[20] B. Endtmayer, U. Langer, T. Wick, "Multigoal-oriented error estimates for non-linear problems", *J. Numer. Math.* **27** (2019), no. 4, p. 215-236.

[21] B. Endtmayer, U. Langer, I. Neitzel, T. Wick, W. Wollner, "Multigoal-oriented optimal control problems with nonlinear PDE constraints", *Comput. Math. Appl.* **79** (2020), no. 10, p. 3001-3026.

[22] B. Endtmayer, *Multi-goal oriented a posteriori error estimates for nonlinear partial differential equations*, PhD Thesis, Johannes Kepler University Linz, Austria, 2021.

[23] S. Beuchler, B. Endtmayer, T. Wick, "Goal oriented error control for stationary incompressible flow coupled to a heat equation", *PAMM* **21** (2021), no. 1, article no. e202100151.

[24] K. Ahuja, B. Endtmayer, M. C. Steinbach, T. Wick, "Multigoal-oriented error estimation and mesh adaptivity for fluid–structure interaction", *J. Comput. Appl. Math.* **412** (2022), article no. 114315.

[25] R. Becker, R. Rannacher, "An optimal control approach to a posteriori error estimation in finite element methods", *Acta Numer.* (2001), p. 1-102.

[26] W. Bangerth, R. Rannacher, *Adaptive Finite Element Methods for Differential Equations*, Lectures in Mathematics, Birkhäuser, 2003.

[27] J. T. Oden, S. Prudhomme, "Estimation of Modeling Error in Computational Mechanics", *J. Comput. Phys.* **182** (2002), no. 2, p. 496-515.

[28] M. Braack, A. Ern, "A posteriori control of modeling errors and discretization errors", *Multiscale Model. Simul.* **1** (2003), no. 2, p. 221-238.

[29] R. Rannacher, J. Vihharev, "Adaptive finite element analysis of nonlinear problems: balancing of discretization and iteration errors", *J. Numer. Math.* **21** (2013), no. 1, p. 23-61.

[30] B. Endtmayer, U. Langer, T. Wick, "Reliability and Efficiency of DWR-Type A Posteriori Error Estimates with Smart Sensitivity Weight Recovering", *Comput. Methods Appl. Math.* **21** (2021), no. 2, p. 351-371.

[31] T. Richter, T. Wick, "Variational localizations of the dual weighted residual estimator", *J. Comput. Appl. Math.* **279** (2015), p. 192-208.

[32] B. Endtmayer, U. Langer, T. Wick, "Two-Side a Posteriori Error Estimates for the Dual-Weighted Residual Method", *SIAM J. Sci. Comput.* **42** (2020), no. 1, p. A371-A394.

[33] S. Arrhenius, “Über die Reaktionsgeschwindigkeit bei der Inversion von Rohrzucker durch Säuren”, *Zeitschrift für Physikalische Chemie* **4U** (1889), no. 1, p. 226-248.

[34] S. Arrhenius, “Über die Dissociationswärme und den Einfluss der Temperatur auf den Dissociationsgrad der Elektrolyte”, *Zeitschrift für Physikalische Chemie* **4U** (1889), no. 1, p. 96-116.

[35] J. De Guzman, “Relation between fluidity and heat of fusion”, *Anales Soc. Espan. Fis. Y. Quim* **11** (1913), p. 353-362.

[36] C. V. Raman, “A theory of the viscosity of liquids”, *Nature* **111** (1923), no. 2790, p. 532-533.

[37] E. N. d. C. Andrade, “LVIII. A theory of the viscosity of liquids.—Part II”, *London, Edinburgh Dublin Philos. Mag. J. Sci.* **17** (1934), no. 113, p. 698-732.

[38] A. G. Ward, “The viscosity of pure liquids”, *Trans. Faraday Soc.* **33** (1937), p. 88-97.

[39] R. B. Haj-Kacem, N. Ouerfelli, J. V. Herráez, M. Guettari, H. Hamda, M. Dallel, “Contribution to modeling the viscosity Arrhenius-type equation for some solvents by statistical correlations analysis”, *Fluid Phase Equilib.* **383** (2014), p. 11-20.

[40] K. R. Rajagopal, M. Ruzicka, A. R. Srinivasa, “On the Oberbeck–Boussinesq approximation”, *Math. Models Methods Appl. Sci.* **6** (1996), no. 8, p. 1157-1167.

[41] R. K. Zeytounian, “Joseph Boussinesq and his approximation: a contemporary view”, *C. R. Méc. Acad. Sci. Paris* **331** (2003), no. 8, p. 575-586.

[42] T. Guerra, A. Sequeira, J. Tiago, “Existence of optimal boundary control for the Navier–Stokes equations with mixed boundary conditions”, *Port. Math. (N.S.)* **72** (2015), no. 2-3, p. 267-283.

[43] P. G. Ciarlet, *The finite element method for elliptic problems*, 2. pr. ed., North-Holland, 1980.

[44] D. Arndt, W. Bangerth, T. C. Clevenger, D. Davydov, M. Fehling, D. Garcia-Sanchez, G. Harper, T. Heister, L. Heltai, M. Kronbichler, R. M. Kynch, M. Maier, J.-P. Pelteret, B. Turcksin, D. Wells, “The `deal.II` Library, Version 9.1”, *J. Numer. Math.* **27** (2019), p. 203-213.

[45] D. Arndt, W. Bangerth, D. Davydov, T. Heister, L. Heltai, M. Kronbichler, M. Maier, J.-P. Pelteret, B. Turcksin, D. Wells, “The deal.II finite element library: Design, features, and insights”, *Comput. Math. Appl.* (2020).

[46] T. A. Davis, I. S. Duff, “An unsymmetric-pattern multifrontal method for sparse LU factorization”, *SIAM J. Matrix Anal. Appl.* **18** (1997), no. 1, p. 140-158.

[47] R. Becker, R. Rannacher, “Weighted a posteriori error control in FE methods”, in *ENUMATH’97* (H. G. Bock *et al.*, eds.), World Scientific, 1996, p. 1-16.

[48] D. Meidner, R. Rannacher, J. Vihharev, “Goal-oriented error control of the iterative solution of finite element equations”, *J. Numer. Math.* **17** (2009), no. 2, p. 143-172.

[49] V. Dolejší, O. Bartoš, F. Roskovec, “Goal-oriented mesh adaptation method for nonlinear problems including algebraic errors”, *Comput. Math. Appl.* **93** (2021), p. 178-198.

[50] F. Tröltzsch, *Optimale Steuerung partieller Differentialgleichungen-Theorie, Verfahren und Anwendungen*, 2nd ed., Vieweg und Teubner; Springer, 2009.

[51] M. Hinze, R. Pinnau, M. Ulbrich, S. Ulbrich, *Optimization with PDE constraints*, Mathematical modelling: theory and applications, no. 23, Springer, 2009.

[52] G. Allaire, “A review of adjoint methods for sensitivity analysis, uncertainty quantification and optimization in numerical codes”, *Ingénieurs de l’Automobile, SIA* **836** (2015), p. 33-36, HAL Id: hal-01242950.

[53] G. Allaire, *Conception optimale de structures*, Mathematiques et applications, vol. 58, Springer, 2006.

[54] M. P. Bruchhäuser, K. Schwegler, M. Bause, “Dual weighted residual based error control for nonstationary convection-dominated equations: potential or ballast?”, in *Boundary and Interior Layers, Computational and Asymptotic Methods BAIL 2018*, Letures Notes in Computational Science and Engineering, vol. 135, Springer, 2020, p. 1-17.

[55] M. Braack, T. Richter, “Solutions of 3D Navier—Stokes benchmark problems with adaptive finite elements”, *Comput. Fluids* **35** (2006), no. 4, p. 372-392.

[56] G. F. Carey, J. T. Oden, *Finite Elements. Computational Aspects*, The Texas Finite Element Series, vol. III, Prentice-Hall, 1984.

[57] W. C. Rheinboldt, C. K. Mesztenyi, “On a data structure for adaptive finite element mesh refinements”, *ACM Trans. Math. Softw.* **6** (1980), no. 2, p. 166-187.

[58] W. Bangerth, O. Kayser-Herold, “Data structures and requirements for hp finite element software”, *ACM Trans. Math. Softw.* **36** (2009), no. 1, article no. 4.

[59] B. Endtmayer, U. Langer, J. Thiele, T. Wick, “Hierarchical DWR Error Estimates for the Navier-Stokes Equations: h and p Enrichment”, in *Numerical Mathematics and Advanced Applications ENUMATH 2019*, Lecture Notes in Computational Science and Engineering, vol. 139, Springer, 2021, p. 363-372.

[60] R. Hartmann, P. Houston, “Goal-oriented a posteriori error estimation for multiple target functionals”, in *Hyperbolic problems: theory, numerics, applications*, Springer, 2003, p. 579-588.

[61] D. Estep, M. Holst, M. Larson, “Generalized Green’s Functions and the Effective Domain of Influence”, *SIAM J. Sci. Comput.* **26** (2005), no. 4, p. 1314-1339.

[62] D. Pardo, “Multigoal-oriented adaptivity for *hp*-finite element methods”, *Procedia Computer Science* **1** (2010), no. 1, p. 1953-1961.

[63] J. Alvarez-Aramberri, D. Pardo, H. Barucq, “Inversion of Magnetotelluric Measurements Using Multigoal Oriented *hp*-adaptivity”, *Procedia Computer Science* **18** (2013), p. 1564-1573.

[64] K. Kergrene, S. Prudhomme, L. Chamoin, M. Laforest, “A new goal-oriented formulation of the finite element method”, *Comput. Methods Appl. Mech. Eng.* **327** (2017), p. 256-276.

[65] K. Kergrene, *A Goal-Oriented Finite Element Method and Its Extension to PGD Reduced-Order Modeling*, PhD Thesis, Ecole Polytechnique, Montreal, (Canada), 2018.

[66] B. Endtmayer, T. Wick, “A Partition-of-Unity Dual-Weighted Residual Approach for Multi-Objective Goal Functional Error Estimation Applied to Elliptic Problems”, *Comput. Methods Appl. Math.* **17** (2017), no. 2, p. 575-599.

[67] M. Schäfer, S. Turek, F. Durst, E. Krause, R. Rannacher, “Benchmark computations of laminar flow around a cylinder”, in *Flow simulation with high-performance computers II*, Notes on Numerical Fluid Mechanics, vol. 48, Springer, 1996, p. 547-566.

[68] D. Perevoznik, A. Tajalli, D. Zuber, W. M. Pätzold, A. Demircan, U. Morgner, “Writing 3D Waveguides With Femtosecond Pulses in Polymers”, *J. Lightwave Technol.* **39** (2021), no. 13, p. 4390-4394.

[69] B. Endtmayer, U. Langer, T. Wick, “Multiple goal-oriented error estimates applied to 3d non-linear problems”, *PAMM* **18** (2018), no. 1, article no. e201800048.